Novel position reconstruction for highly granular electromagnetic calorimeters

Brendon Madison[1,*] and *Graham* Wilson[1]

[1]Department of Physics and Astronomy, University of Kansas, Lawrence, KS 66045, USA

Abstract. We present work on design and reconstruction methods for sampling electromagnetic calorimeters with emphasis on highly granular designs. We use the clustered logarithmically weighted center-of-gravity (lwk-means) for benchmarking position resolution. We find that θ and ϕ resolution for high energy photons in Si-W designs improves with increasing both sampling frequency and sampling thickness. Augmenting only one is found to have mixed results. We find that lwk-means is unable to effectively use calorimeter transverse cell sizes smaller than 2 mm. New reconstruction methods for highly granular designs are developed. We find that methods that only measure the initial particle shower and disregard the remaining shower can take advantage of cell sizes down to at least 10 μm significantly outperforming the benchmark method. Of these, the best method and design is the initial particle shower "single hit", method using the calorimeter design with the highest sampling frequency and sampling thickness.

1 Introduction

We have been working on a new approach to forward calorimetry for luminosity measurement at a future high energy e^+e^- collider using both Bhabha scattering and the $e^+e^- \to \gamma\gamma$ process. Further motivation can be found in other work [1]. We note here that improving angular measurements of Bhabhas and $\gamma\gamma$ is important for luminosity systematics and that $\gamma\gamma$ is important for addressing beam biases present in Bhabhas [1]. This has focused our attention on how well one can reconstruct high energy electromagnetic showers and in particular those of high energy photons using dedicated electromagnetic calorimeters (ECALs). This application emphasizes high performance energy resolution, polar angle resolution, and azimuthal angle resolution. In the present work, the focus is on position/angle resolution.

In ECAL design, designs that are highly segmented longitudinally typically have high values of Molière radius (R_M), corresponding to thelateral spread of an electromagnetic shower being large. This metric is used as a rule-of-thumb for determining the likely quality of position or angle reconstruction of a calorimeter design [2]. It is considered inversely correlated to position/angle resolution. However, as we shall demonstrate in Sect. 3 and Sect. 4, the ultimate position/angle resolution is more related to how well one can construct the interactions associated with the initial shower components.

The Molière radius is measured with respect to the shower axis, which is the center-of-gravity (CoG) of the shower along the direction the shower proceeds. In a sandwich calorimeter, with square cells, there is measurement bias in the CoG that arises when the shower is

*e-mail: brendon_madison@ku.edu

at an angle with respect to the surface of the calorimeter. For this reason it is necessary to measure the particle shower angle before the CoG as the calorimeter measurements must be rotated to correct for this bias. A demonstration of this can be seen in figure 1, wherein the CoG bias from angles of incidence of the particle shower has been simulated for a toy detector concept.

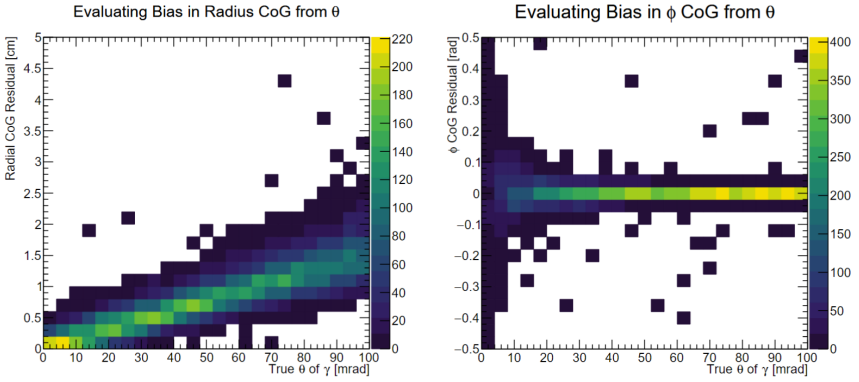

Figure 1. Center-of-gravity bias in radius and ϕ measurements given various values of θ and using 128 GeV photons. This detector simulation was done with a detector displacement from the initial particle position of 2.5 meters. The simulation includes a 3.5T magnetic field. The detector is a sandwich design with cells in the x-y plane and layers along the z axis.

We observe the expected bias in that the bias in radius, for small angles, scales linearly with θ and that there is no bias in ϕ with respect to θ value. For the variance of the resolution we observe that the ϕ variance scales with θ^{-1} while R variance of resolution is constant in θ.

Originally the Molière radius was characterized by the cylindrical radius, about the shower axis, which contains 90% of the deposited energy of the particle shower [3]. The Molière radius can span large values for various experiments, where SiW (Silicon-Tungsten) sandwich will be close to the R_M of Tungsten of 9.33 cm while air shower experiments are near 73.30 meters. For ECALs made of mixtures of materials the Molière radius can be computed from references with respect to the electromagnetic scale energy (E_s) as

$$R_M = E_s \left[\sum_j \frac{w_j E_{cj}}{X_{0j}} \right]^{-1} \approx \left[\sum_j \frac{w_j}{R_{Mj}} \right]^{-1} \tag{1}$$

where the radiation length weights, w_j, of each material is used with respect to its electron critical energy E_{cj} and radiation length X_{0j} [4]. We provide an additional approximation that depends on the material specific Molière radius of R_{Mj} [5]. Note that equation 1 must be computed using the density form, units of $\frac{mass}{area}$ of R_{Mj} , not the length form. Not taking this into account will result in the densest material erroneously dominating the calculation.

We can compare R_M of two different calorimeter designs by using equation 1. We compare two candidate forward calorimeters, the International Large Detector (ILD) Luminosity Calorimeter (LumiCal) and a work-in-progress proposed new forward calorimeter. This work-in-progress will have 240 layers of $\frac{1}{6}X_0$ SiW , with 1 mm thick silicon. LumiCal uses 30 layers of $1X_0$ SiW, with 0.3 mm thick silicon. For simplicity, we evaluate both of these as

square calorimeters, that is to say segmented uniformly in the x-axis and y-axis. We note that ILD LumiCal is segmented in rϕ, into layers of "towers" [5].

Using equation 1 and references we find that ILD LumiCal's Molière radius is 14.7 mm while the proposed design is 41.4 mm [5]. This is different from the measured value of 9.46 mm used in the LumiCal reference as we are using a simplified version of LumiCal and not an effective Molière radius.

2 Benchmark estimators

2.1 Center of gravity

As established in Sect. 1, to best use methods like CoG or clustering one must remove any angular bias. To remove angular bias one may use angular, i.e. θ or ϕ, CoG. This is often accented by the use of clustering.

The standard CoG method is, mathematically, an average spanning the members of that space. E.g. the CoG for hits along the x-axis is simply the average value of hits along the x-axis. If the CoG is weighted, say by energy, then the user scales the x-axis according to the hit energies, similar to spatial curvature if one wants to maintain the curved space analogy, and computes the energy weighted average.

As a step-up from the standard or energy weighted CoG is the log-weighted CoG. Previous work has shown that it is less biased and better resolution for laterally segmented detectors [6]. Here we write the general form of log-weighted weights as

$$w_j = \mathrm{Max}\left[\quad 0 \quad , \quad W_0 + \log\left(w_{ini,j} x_j \left[\sum_j w_{ini,j} \right]^{-1} \right) \quad \right] \tag{2}$$

with dependence on a free parameter W_0, that is to be determined later. The initial weights of equation 2, $w_{ini,j}$, are determined by the user. The parameter W_0, when using the general form of equation 2, acts as a cut on the initial weights. When W_0 is small, or correspondingly the value of $\sum_j w_{ini,j}$ is large comparative to the average value of $w_{ini,j}$, hits are given zero weight. Meaning that they are disregarded in the average. This can prove to be problematic in the limit of a large number of hits and low variance in the hit weights. Where the parameter of W_0 will, by the form of $\log\left(w_{ini,j} x_j \left[\sum_j w_{ini,j} \right]^{-1} \right)$ in equation 2 also become a cut on the number of allowed hits. E.g. for 100 minimum ionizing particles (MIPs) with exactly average hit energies, any value of $W_0 < 2$ will return all zero weights for all hits.

Typically the hit energy, E_j, is used for $w_{ini,j}$ and the weights of equation 2. Therefore the log-weighted energetic CoG is slightly more complicated than linear weighting. Given this, the value of W_0 in equation 2 acts like both a cut on number of allowed weighted hits and as an energy threshold. Since energetic weights in equation 2 couples the number and energies of hits with their final weights.

2.2 Clustering

A common clustering algorithm is the k-means algorithm. It is attractive as it is simple and fast. K-means relies on random number generation, and so is sometimes disfavored over concerns that it does not generate exactly reproducible solutions or that this randomness cannot handle complex data. Despite these concerns, extensive studies have shown that k-means reliably converges to optimal solutions within less than 100 iterations outside of special circumstances [7]. Considering this, and that the data here does not meet any referenced circumstances, we find no reason to be concerned with using k-means here [7].

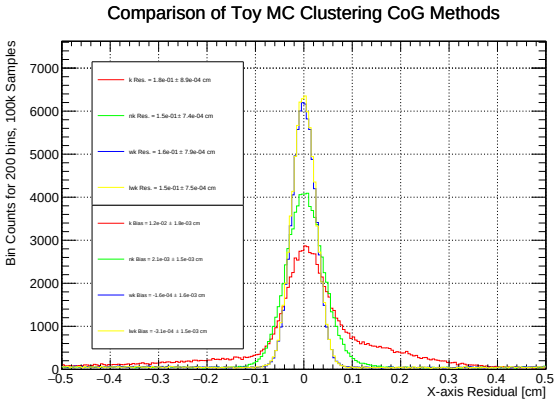

Figure 2. X-axis residual results for various combinations of clustering and CoG methods. This was done using the toy MC as described in Subsect 2.2. For conciseness each combination label has been shortened such that k-means is k, nk-means is nk, wk-means is wk and lwk-means is lwk.

As a part of the k-means algorithm the distance between a hit and all of possible hits is computed. This is done to determine what hits to cluster and which hits to add to which clusters. When dealing with two dimensional data with identical range and variance there is no bias in k-means clustering. Generally, these two constraints are not true and thus there is bias in the k-means clustering [8]. To remedy this normalized k-means, known as n-k-means, is used [8]. The normalization is done according to range, and not integral, so the range of values lies within $[0, 1]$.

K-means computes centroids, i.e. averages, for clusters during assigning hits to clusters. Centroids are typically computed using an unweighted averaging, i.e. an unweighted CoG method as done in Subsect. 2.1. We may expand the k-means CoG to use weighted methods such that we have weighted k-means, wk-means, and log-weighted k-means, lwk-means.

We test the combinations of these different CoG approaches and clustering. The experimental approach is to use a toy MC. We simulate three clusters that are chosen about the circumference of a circle that is centered in x,y at (0,0). So that the average of the clusters should give (0,0). The radius of the circle is chosen by a uniform random from a value from 1 cm to 3 cm. Then three angles are chosen for the clusters such that they are equal angle from each other. That is to say, each cluster is angularly separated by $\frac{2\pi}{3}$ radians. Then 72 hits are generated, with 12 for the first cluster, 24 for the second cluster and 36 for the third cluster. Each cluster is also given a different variance in spatial distribution that is consistent across each trial of the simulation. Each hit is given a Gaussian weighting, to simulate energy weighting, that is maximal at the center of the cluster. The y-axis values are also scaled by a factor of three to simulate the reality that the clustering axes may not be similar in scale. After this, the position values were digitized to the centers of 100 micron cells. This simulation was then run for 100k trials.

To evaluate resolution the single axis resolution was computed from the residual of the CoG of the clusters with respect to the origin. We then numerically evaluate the resolution using the 2σ interquantile range (IQR) of the residuals. For this range this method of error evaluation is known as IQR95, from the Gaussian confidence interval. These are then rescaled by $\frac{1}{2}$ to be the 1σ quantile. The bias is evaluated using the 0.5 quantile of the residuals.

We investigate the single axis, using the x-axis, resolution to evaluate bias and resolution. As seen in figure 2, lwk-means performs best in resolution, roughly 10% better than wk-means. We also observe that lwk-means has a larger bias than wk-means, but the bias in both is smaller than the uncertainty. Meaning that both are, for this test size, unbiased. If bias and resolution are combined quadratically, lwk-means is the superior method. This result also

finds that the resolution is larger than the intrinsic resolution. So there is a need to find better methods in order to reach the intrinsic resolution.

3 Results for chosen benchmark estimator

Following the results of Sect. 2.2, and the results of other sources, we have chosen to use lwk-means as the benchmark for this section [6]. For testing this method we have simulated, in GEANT4, four designs. Two $1X_0$ designs and two $\frac{1}{6}X_0$ designs. Each design is simulated with both a silicon thickness of 0.3 mm and 1 mm. The simulation was done with fixed angles of θ of 50 mrad and ϕ of $\frac{\pi}{4}$. We chose not to use test beam geometry, where the angles are set to zero, as the bias observed in figure 1 shows that this case would be poorly representative of typical function. The initial particle was chosen to be a 128 GeV γ so that these results can be applied to future studies of $\gamma\gamma$ luminosity studies at various energies that are spaced according to $\log_2(E)$. The materials used in the detector were a passive layer of tungsten, an active layer of silicon, 1 mm of PCB (G10) and 1 mm of air gap. The detector was offset by 2.5m from the beam origin in order to be comparable to the ILD forward calorimeter region [9].

This is done with numerous values of different cell sizes for the silicon active layer. Digitization is done after GEANT4 is ran such that the generator level information of the steps in GEANT4 are stored and then digitized afterwards based off of the specifications of the cells that the user wants. This was done to avoid geometry limit issues and memory issues that can arise in GEANT4 when one tries to simulate numerous layers of small, $\leq$100 μm, cells. There is also a possibility of charge sharing but the work shown here does not include any charge sharing of nearby pixels.

For this particular simulation, since there are no "towers" as there are in the ILD LumiCal design, instead the initial clustering is done in layers [5]. As in the ILD LumiCal reconstruction, clustering is then repeated in these segments, again here layers instead of "towers", and then repeated across layers until there is one centroid. This centroid, i.e. final CoG, is then treated as the measurement. We also use the same optimized value of $W_0 = 3.4$ as is done elsewhere [6].

Investigating the results of figures 3 and 4, we may model the change in performance for a given detector design, using a CoG approach such as in this section, as follows. We propose that the position resolution

$$\sigma_{res.} \sim \frac{R_M}{\sqrt{f_{samp.}}} \tag{3}$$

depends on the Molière radius and the sampling fraction, $f_{samp.}$, which is unitless. This model is not new and calorimeter design references note the dependence on these factors [10].

Computing the Molière radius for a composite material, as done in Sect. 1, reveals that the Molière radius depends on the sampling frequency, $\mathcal{N}$, in units of $\frac{samples}{X_0}$. Such that

$$R_M \sim \frac{1}{\mathcal{N}} \tag{4}$$

the Molière radius is inversely related to the sampling frequency. We can also relate the sampling fraction to the thickness of the active component and passive component [10]. The sampling fraction is defined

$$f_{samp.} = \frac{E_{act.}}{E_{pas.} + E_{act.}} \approx \frac{dE_{act.}}{dx} d_{act.} \left[\frac{dE_{act.}}{dx} d_{act.} + \frac{dE_{pas.}}{dx} d_{pas.} \right]^{-1} \tag{5}$$

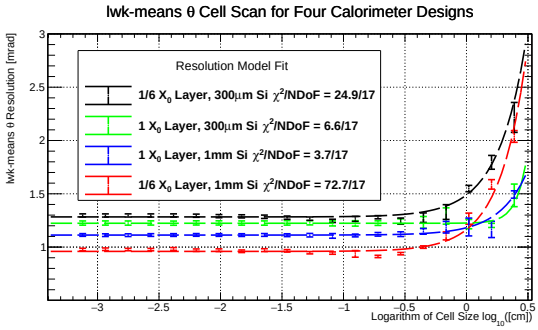

Figure 3. Results of cell scan of θ resolution using four calorimeter designs to use as reference. The estimator used is the log-weighted k-means, lwk-means, method. We observe that the designs with thicker silicon are superior for θ resolution. The fit corresponds to a parameterized form of equation 9.

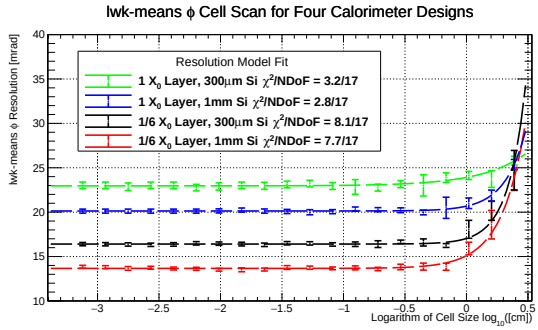

Figure 4. Results of cell scan of ϕ resolution using four calorimeter designs. The reconstruction method used is the log-weighted k-means, lwk-means, method. We observe that designs with higher sampling frequency are superior for ϕ resolution. The fit corresponds to a parameterized form of equation 9.

as depending on the energy deposited in the active and passive layers. This is typically done by choosing a specific physics process, namely MIPs [10]. For said physics process there is a known energy per length differential of $\frac{dE}{dx}$ which typically varies for different materials and thus the different notation for the active and passive materials. The sampling fraction, when the thickness of the active layer is held constant,

$$\lim_{d_{act.}=const.} f_{samp.} \sim \frac{1}{\mathcal{N}} \tag{6}$$

follows an inverse relationship with the sampling frequency. We then rewrite equation 5 in terms of the thickness of the active component, $d_{act.}$, the thickness of the passive component, $d_{pas.}$ and the sampling frequency. By using equations 4, 5 and 6, we rewrite equation 3

$$\sigma_{res.} \sim \sqrt{\frac{d_{pas.}}{d_{act.}\mathcal{N}^3}} \tag{7}$$

to show how it compares to dependence on the thickness of the active layer and the sampling frequency. We note that the position resolution is dependent on $\frac{1}{\sqrt{f_{samp.}}}$, which is similar to the dependence seen in energy resolution [10]. Upon examining the energy resolutions from GEANT4 simulations, as seen in table 1, that energy resolution, $\mathcal{E}$

$$\mathcal{E} \sim \sqrt{\frac{d_{pas.}}{d_{act.}\mathcal{N}}} \tag{8}$$

has similar dependence to the position resolution, but with a smaller power of sampling frequency in the denominator. Using equation 8 we can note that equation 7 is equivalent to $\sigma_{res.} \sim \frac{\mathcal{E}}{\mathcal{N}}$, having dependence on energy resolution. This energy resolution dependence

Table 1. A selection of the four electromagnetic calorimeter designs with measured electromagnetic deposited energy fractions and energy resolution for 128 GeV photons. All calorimeters are sufficiently deep to guarantee longitudinal containment (here $40X_0$.)

Energy Resolution			
Layer Design	Si Thickness [mm]	EM Fraction	Energy Resolution
$1\ X_0$	0.3	0.964%	$18.4\%/\sqrt{E}$
$1\ X_0$	1	3.31%	$15.7\%/\sqrt{E}$
$\frac{1}{6}\ X_0$	0.3	5.21%	$6.6\%/\sqrt{E}$
$\frac{1}{6}\ X_0$	1	17.0%	$4.8\%/\sqrt{E}$

agrees with current standards [10]. We can expand this further, to include effects from lateral cell size, d_{cell}, as has been shown by previous work [11]. Thus equation 7 is rewritten to

$$\sigma_{res.} \sim \frac{\mathcal{E}}{\mathcal{N}} \oplus e^{d_{cell}} \tag{9}$$

which has an exponential dependence on cell size. To keep the argument of the exponential function unitless, d_{cell} is measured in terms of interaction lengths [11]. This term is added in quadrature such that, for methods or designs that become limited by other factors, smaller cell sizes do not improve performance. This exponential trend in cell size is observed as a linear trend in the log plots of figures 3 and 4.

Fitting the cell scan plots seen in figures 3 and 4 to a parameterized form of equation 9 finds that the fit quality is plausible for the $1\ X_0$ designs but questionable for the $\frac{1}{6}X_0$ designs. Particularly the fit of the $\frac{1}{6}X_0$ designs is poor around the 5 mm cell size area. As a part of the fitting process the parameter used to represent the $\mathcal{E}/\mathcal{N}$ term was held constant amongst fits for the same design. This term was also held constant in terms of the expected ratio from the design values of $\mathcal{E}/\mathcal{N}$ used. To address the poor quality of fit for the $\frac{1}{6}X_0$ designs we propose

$$\sigma_{res.} \sim \frac{\mathcal{E}}{\mathcal{N}} \oplus (e^{d_{cell}} + \mathcal{N}e^{d_{cell}^2}) \tag{10}$$

an exponential expansion of the cell size dependent term that is dependent on the sampling frequency. By introducing this term, and scaling with sampling frequency, the new term is expected to only be significant in the $\frac{1}{6}X_0$ designs.

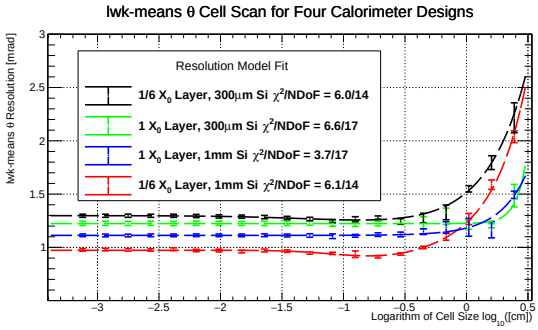

Figure 5. Following figure 3, we repeat the cell size scan of θ for the new model of equation 10 for the $\frac{1}{6}X_0$ designs. The new model brings the quality of fits to being comparable to previous fits for $1\ X_0$ designs.

We repeat the fitting process, as done before in figures 3 and 4, with the updated model of equation 10. The results, as seen in figures 5 and 6, indicate that the new model is plausible. We did not test the $1\ X_0$ designs for the new model as the additional term is assumed to be too small to impact the fit. During the fitting process the parameter that scales with sampling

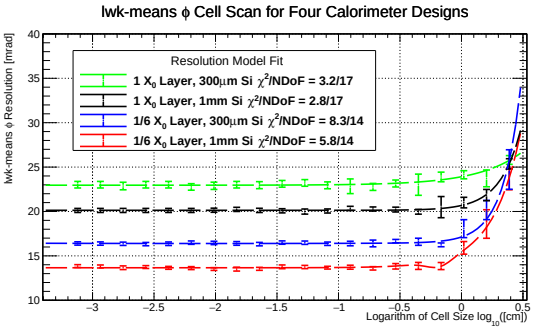

Figure 6. Following figure 4, we repeat the cell size scan of ϕ for the new model of equation 10 for the $\frac{1}{6}X_0$ designs. The new model brings the quality of fits for the $\frac{1}{6}X_0$ designs to being plausible.

frequency was held constant for all the fits, to reflect the fact that the model would also require this consistency across the different $\frac{1}{6}X_0$ designs. So that the dependence on sampling frequency is also plausible and consistent.

During the evaluation of fits it was determined that this additional factor influences the resolution by roughly 0.2%. As such, the assumption that this effect is too small in the 1 X_0 designs is plausible as the data uncertainty is comparable to 0.1%. One would need considerable increase in data precision as this effect is already small in the $\frac{1}{6}X_0$ designs. Given these results equation 10 is a plausible model for position resolution when incident particle energy is fixed and one only varies sampling frequency and sampling fraction.

To determine how well a pairing of calorimeter design and reconstruction technique does at exploiting the cell size being used, we introduce $d_{min.}$, the point at which the pairing reaches a minima resolution. We refer to this as the minimum cell size a.k.a. minimum pitch. By its design, $d_{min.}$ is also the point at which smaller cell size no longer positively impacts the quality of reconstruction. Therefore knowing the value of the minimum pitch for a particular pairing can be useful for informing the design of the cell size used for a given calorimeter design.

The minimum pitch values were found using the fits seen in figures 5, 6 and then compiled into table 2. This table also features the minimum resolution values as found using the lwk-means method with the various designs. Examining the resolution values reveals that there is no shared ordering for the designs in terms of quality of resolution between θ and ϕ for the lwk-means reconstruction. Instead it seems that increasing sampling frequency is more impactful for ϕ resolution while increasing sampling fraction is more impactful for θ resolution. Increasing both simultaneously, as done in the $\frac{1}{6}X_0$ and 1 mm silicon design, has the benefits of both improvements and is the best design for position resolution in both angles.

The results of table 2 also indicate that the cell size does not have significant effect on lwk-means reconstruction below 2 mm in cell size. As such, lwk-means reconstruction is not desirable in circumstances where one wishes to use smaller cell sizes to achieve higher resolution. Lwk-means reconstruction is suitable for large cell sizes where it is able to approach the $\frac{d}{\sqrt{12}}$ fundamental geometric cell resolution limit. We can test this by noting that the geometric cell resolution limit for θ

$$\sigma_\theta = \frac{d}{z_{offset}\sqrt{12}} \tag{11}$$

depends on the transverse cell size, d, and the offset of the calorimeter from the interaction point along the z-axis, z_{offset}. As an example, for the $\frac{1}{6}X_0$ and 1 mm silicon design equation 11 would be roughly 0.6 mrad. Which is slightly smaller than the value of 0.98 mrad observed in table 2.

Table 2. Extrapolated minimum pitch given the fits seen in figures 5 and 6. Values are calculated using the fits of said figures. These results are representative of their listed designs and the lwk-means reconstruction method.

Minimum Pitch for lwk-means Reconstruction			
Design	Variable	Resolution [mrad]	Minimum Pitch ($d_{min.}$) [mm]
$\frac{1}{6}$ X_0 , 0.3 mm Si	θ	1.30 ± 0.01	5.3 ± 0.5
1 X_0 , 0.3 mm Si	θ	1.22 ± 0.01	3.6 ± 0.4
1 X_0 , 1 mm Si	θ	1.11 ± 0.01	2.0 ± 0.3
$\frac{1}{6}$ X_0 , 1 mm Si	θ	0.98 ± 0.01	4.3 ± 0.4
1 X_0 , 0.3 mm Si	ϕ	23.0 ± 0.2	29 ± 3
1 X_0 , 1 mm Si	ϕ	20.1 ± 0.2	6.9 ± 0.7
$\frac{1}{6}$ X_0 , 0.3 mm Si	ϕ	16.5 ± 0.2	4.7 ± 0.5
$\frac{1}{6}$ X_0 , 1 mm Si	ϕ	13.7 ± 0.2	5.1 ± 0.5

We warrant the result of lwk-means reconstruction with three conditions. Other cell designs, such as $r\phi$ cells, can be used and they may be more advantageous for lwk-means. The lwk-means method also has numerous parameters that can be further tuned for these particular designs, which was not exhaustively done here. In addition to this algorithmic tuning it is also common to have weights for layers, both depending on the shower shape and quality of the layer's measurement, such as done in OPAL's luminosity measurement [12].

3.1 Projecting results

Given the results of Sect. 3, the GEANT4 simulations and the resolution models provide a starting point for further extrapolation for the purpose of determining optimal calorimeter design. In particular, we may choose to use equation 3 as a starting point since it depends on the Molière radius and sampling fraction. Both of which can be estimated by using calorimeter design values and material reference values.

A computer script was written to perform this projection. The results were taken a relative with respect to values from the 1 X_0 and 0.3 mm silicon design. This projection was given three constraints for possible projected designs with particular emphasis on constraining to a design that is feasible for the forward calorimeter region of ILD [9]. Designs that exceed 1 m in total length are vetoed to respect the space of the forward calorimter region [9]. We have also constrained the sampling frequency to be greater than 0.5, as the performance drastically decreases below this point. The maximum cell thickness was constrained to 1.8 mm in order to keep possible designs within ranges that have been experimentally tested in other work [13].

The results, as seen in figure 7, indicates that the ordering and magnitudes of resolutions, as seen in table 2, are not consistent with the projection. However, it is not expected for the ordering or magnitude of this projection to match as this projection includes only calorimeter design effects and no reconstruction effects.

Considering the results of the projection it is clear that more granular designs are preferential for improving position resolution. The design that uses $\frac{1}{6}X_0$ and 1 mm silicon is not only the best design tested here but performs near the optimal point of the projected designs. Since the performance of the lwk-means reconstruction seen in Sect. 3 does not agree with the significantly better performance for granular designs seen in figure 7, we suspect that new methods, particularly suited for granular designs, need to be developed. To do so we must investigate things that granular designs are suited for.

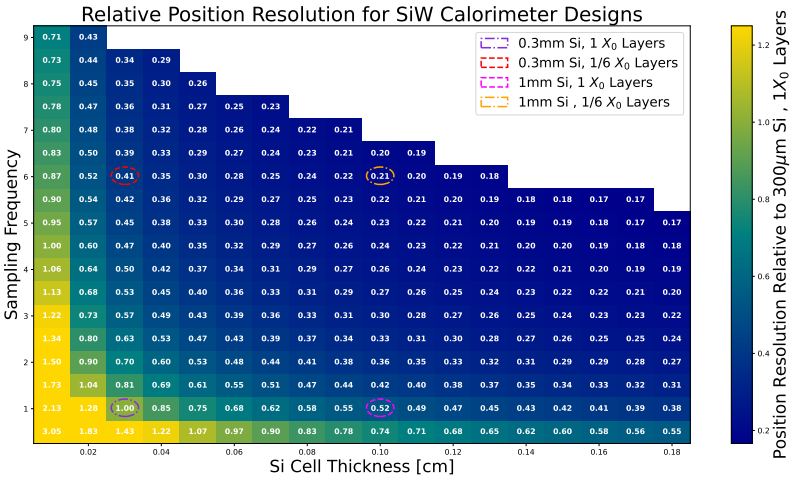

Figure 7. Results of extrapolating out equation 7 for the two degrees of freedom that it has. The sampling frequency scales with the plot y-axis while the sampling fraction is related to the sampling thickness. Four points are marked for reference as the designs being tested in this work.

4 New reconstruction proposal

In a calorimeter designed for tracking the sampling frequency is typically increased compared to calorimeters built for energy resolution where the sampling fraction would be increased instead. The increased sampling frequency allows for numerous measurements to be made of incoming particles with minimal scattering of the incoming particle. We propose to mimic this process for highly granular sampling calorimeter designs by focusing on the initial part of the particle shower. In this regime the shower is not well described by the Molière radius, so we do not expect large values of Molière radius to degrade performance. Instead the shower is characterized by the spread of the photon conversion that starts the particle shower. This is characterized by physics like the Bethe-Heitler process where the opening angle is quite narrow, $\approx 1/\gamma = m_e c^2/E_\gamma$, and inversely related to the incident photon energy [14]. For an incident 128 GeV photon, as used in the GEANT4 simulations done here, this corresponds to a few micro-radians to tens of micro-radians.

4.1 Investigating the initial shower

If we investigate the first five radiation lengths of the particle shower, such as in figure 8, we can see that the structure of the initial shower, and its trajectory, are much clearer in the more granular design. There are numerous layers where the only hits within the window displayed in figure 8 are the ones from the initial shower conversion. By comparison the five layers from the less granular design feature other hits that may not be directly related to the initial shower conversion. The increased number of samples, by virtue of increased sampling frequency, allows for the use of more comprehensive methods like averaging and fitting. The increased number of samples also inherently reduces the statistical error. There

are thus multiple reasons to believe that the granular design can outperform the low sampling frequency design on position resolution.

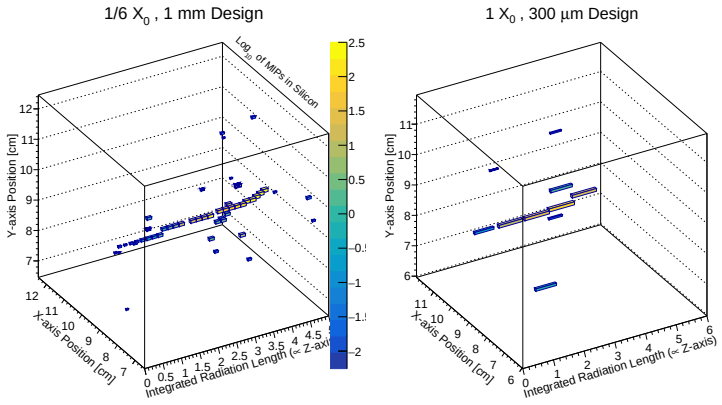

Figure 8. Event display comparing the initial shower for two different events for two different designs. The first five radiation lengths of layers after the shower start are shown for each. Both are 128 GeV γ events that converted in tungsten, have the same incident angles, and are centered on the conversion point along the X-axis and Y-axis positions. The transverse cell sized used for both was 100 μm but the bin sizes are 10 times this, at 1 mm. The plots share one color axis that represents the energy in each bin as the logarithm of the number of MIPs. The integrated radiation length is done relative to the conversion point.

4.2 New methods

For the sake of conciseness we will focus this section on the results for θ resolution.

To begin testing methods of position reconstruction using only the initial particle shower one needs a method to isolate the initial particle shower from the remaining shower. To do this a window is used in terms of the z-axis, or layer number, and the value of θ corresponding to hits in the active layer with respect to the interaction point. We have chosen not to use any windowing in ϕ for this study. Since we anticipate varying the cell size, as done in Sect. 3, we need to choose a value for the θ window that will be small enough to take advantage of the cell size. As such, we have fixed the value of θ for the window to be the equivalent angular spread of three transverse cell sizes, centered on the cell the shower starts in. This value can be calculated using equation 11.

For the purpose of this study we wanted to mainly be sensitive to the underlying calorimeter design and not systematics from the reconstruction method. As such we have "cheated" the values for the true angles of θ and ϕ as well as the position of the start of the electromagnetic shower. By cheating these values we ensure that the windowing is being utilized correctly.

The windowing process starts with applying the cut in θ centered on the true θ value. This windowing cut was scaled according to the transverse cell size such that it would be a three cells in diameter. The remaining hits are then discarded if they exist outside the window. A second cut is applied to hits that occur deeper than the shower maximum energy deposited layer. Of the remaining hits an algorithm, which starts at the earliest, along the z-axis, hit in the electromagnetic shower, checks the subsequent layer for hits. If there are no hits then the algorithm assumes that the initial shower has scattered out of the window and truncates the

sample to those which are before this point. If there are hits in the next layer then it includes these hits with the starting hit and then repeats the process, looking at the next layer for hits. This repeats until it either finds no new hits in the window or it reaches the layer of the shower maximum. At which point it stops and the collected hits are used as representing the initial shower.

The efficiency of this windowing algorithm, done with the four different designs, can be seen in figure 9. We find that, regardless of which design is used, there are a significant number of events that fail to have any hits within the window. This is with exception to a sweet-spot for both granular, $\frac{1}{6}X_0$ layers, designs around the 100 micron transverse cell size. We postulate that this sweet-spot occurs because the equivalent angular spread per layer for these cell sizes approaches 1-10 microradians. This angular spread is similar to the spread expected from either multiple scattering or photon conversion [4] [15]. Due to these sources of angular spread, cells that are even smaller end up with particles of the initial shower not being in the same cell or even being nearest neighbors. Therefore a windowing algorithm that cuts out beyond nearest neighbors, as done here, is cutting out some of the particles of the initial shower. Suggesting that the windowing algorithm needs improvement to handle these other cases. Similar to the results for position resolution in Sect. 3, the best design for window efficiency is almost always the $\frac{1}{6}X_0$ and 1 mm silicon design.

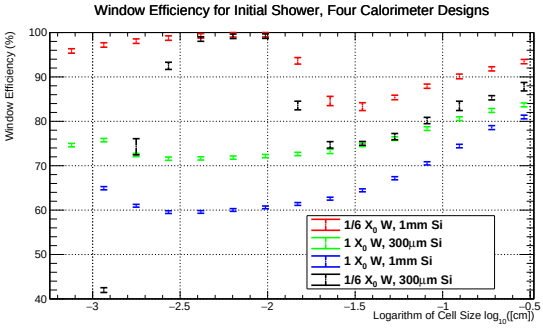

Figure 9. Window efficiency for θ window used for the initial shower reconstruction methods. Events where there are no hits in the silicon within the window after the start of the shower cause the less than 100% efficiency.

Inspired by other work that fits electromagnetic showers, we chose to test both averaging and fitting of the initial particle shower [16]. Both averaging and fitting were tested using unweighted and energy weighted versions. It was found that averaging always resulted in a slightly poorer resolution to fitting. As such we do not present the results of using the averaging reconstruction methods. For notation purposes, we refer to the energetically weighted initial shower fit method as ISE fit and the unweighted initial shower fit as IS fit.

Fitting was done by fitting the θ of the windowed hits to a single parameter of a constant. This was done so that the quality of fit, and the uncertainty of the fitted value, could be used in analysis. The results of the fitted reconstruction methods, as seen in figures 10, have similar linear trends in the log-log plots of resolution and cell size. This is indicative of the exponential term seen in equation 9.

Unlike the results of Sect. 3 we do not see evidence of minimum resolution being reached all the way down to the smallest, roughly 10 μm, cell size tested here. Instead the fitting methods seem to follow the geometric value of $d/\sqrt{12}$. Indicating these reconstruction methods are good for future designs that want to exploit smaller cell sizes. Comparing the two fit methods against each other we find that the unweighted fit performs slightly better. We also observe that the best design is the $\frac{1}{6}X_0$ and 1 mm silicon design.

For the sake of comparison of the fit methods we choose to restrict to 100 micron transverse cell size and use the best design. For 100 micron cells the best design is the $\frac{1}{6}X_0$ and

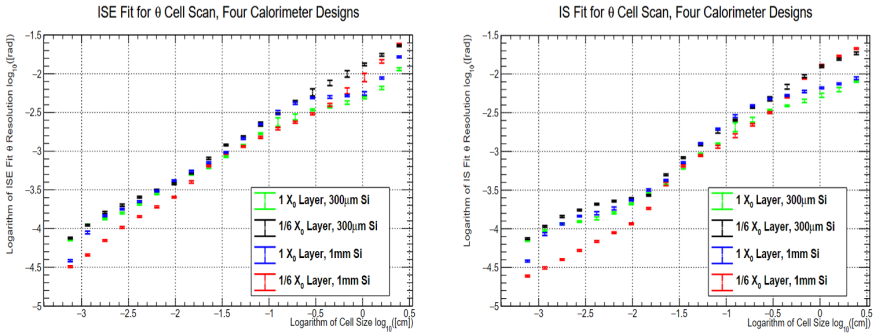

Figure 10. Results of cell scan of θ resolution of IS fit, the unweighted initial shower fit method, and the ISE fit, the energy weighted initial shower fit method. At cell sizes smaller than 100 microns the $\frac{1}{6}X_0$ and 1 mm silicon design is best. Similar performance is observed for both methods.

1 mm design. At this point ISE fit θ has a resolution of 0.22 ± 0.01 mrad conversion and IS fit θ has a resolution of 0.10 ± 0.01 mrad. So the unweighted fit outperforms the energy weighted fit by roughly a factor of two. It should be expected that weighting for energy in the initial shower does not improve performance as it makes the reconstruction sensitive to the particle multiplicity of the initial photon conversion as well as fluctuations in the energy deposited.

As an alternative to the fitting methods we propose a new approach that assumes that we have a method of determining which hit in the initial shower sample has the minimum residual to the true θ value. This method, dubbed the "single hit" method due to it relying on a single hit, uses cheated information so that the method can be evaluated without systematics of the method used in the identification of the single hit. The result of the single hit method, as seen in figure 11, has a significantly different trend from those seen in Sect.3 or for the previous fitting methods.

We observe that the performance of the single hit method is superior to the previous fit methods with a minimum resolution in θ of 2.95 ± 0.05 micro-radians. Figure 11 also shows that, for ϕ resolution, the single hit method can approach 0.1 mrad resolution. The performance is optimal for the 1 mm Si with $1/6$ X_0 layers design around 100 micron transverse cell size. We postulate that this optimal point occurs for similar angular spread reasons that were observed with window efficiency in figure 9. This performance surpasses even the value expected from the geometric limit computed from equation 11. While this is initially unexpected there is a plausible explanation. The single hit method requires sampling numerous points. When the incidence angle of the incident particle is non-zero there is a significant chance that the shower, as it travels through multiple layers, will hit cells that are not perfectly aligned. This staggering in the cells results in

$$d_{eff.} = \frac{d}{N_{IS}} \tag{12}$$

an effective cell size we refer to as $d_{eff.}$. This effective cell size can be reduced by as much as the number of layers in the initial shower, here written as N_{IS}. This staggering can be observed in figure 8, where there are multiple bins in the second layer on the granular calorimeter's event display. We note that equation 12 assumes that the spacing of layers can optimally take advantage of this staggering effect, which is likely not true. Still, this is a

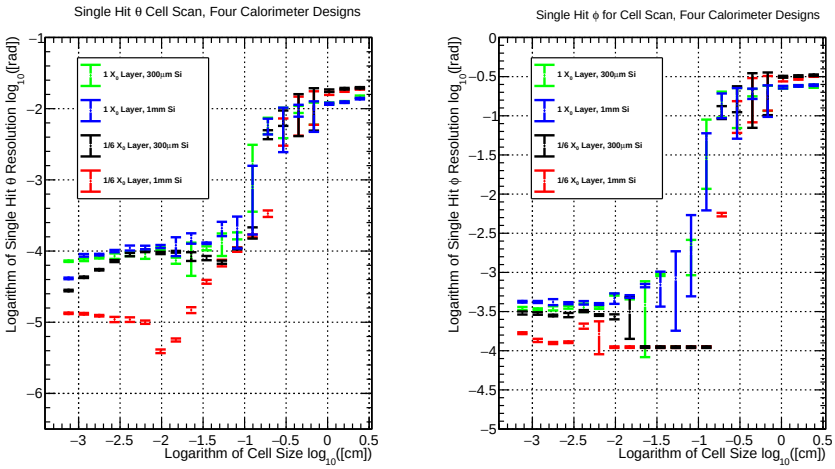

Figure 11. Results of cell scan of θ and ϕ resolutions for the single hit method. At cell size of roughly 100 microns the $\frac{1}{6}X_0$ and 1 mm silicon design is best.

plausible explanation as choosing a single hit bypasses the averaging that gives rise to the typical limit seen in equation 11.

For the single hit method to be viable in a un-cheated analysis a method for identifying the minimum residual hit is needed. More work needs to be done to better understand the staggering effect and how it effects the methods covered in this section.

5 Conclusion and outlook

Related to further studies on forward calorimeter design at future high energy e^+e^- colliders, this work has displayed numerous benefits for calorimeter designs with higher sampling frequency and higher sampling thicknesses. Of all the reconstruction methods tested here, the $\frac{1}{6}X_0$ and 1 mm silicon design, which had both the maximally tested sampling frequency and sampling thickness, outperformed the other designs in both θ and ϕ resolution. This design is also, per our projections of possible calorimeter designs presented in Sect. 3.1, within the forward calorimetry space constraint for future linear colliders and close to optimal position resolution. Our new reconstruction methods, covered in Subsect.4, are capable of approaching, and even surpassing, the typical geometric resolution limit for cell sizes down to, at least, 100 μm. We expect that a staggering effect, which yields a smaller effective cell size, is responsible for the minimum θ resolution for the single hit method of 2.95 ± 0.05 micro-radians. Further work needs to be done to flesh out the new reconstruction methods. Both in terms of improving the windowing process and in terms of making the analysis a purely detector level analysis.

6 Acknowledgements

This work is partially supported by the US National Science Foundation (NSF) under awards NSF 2013007 and NSF 2310030 and benefited from use of the HPC facilities operated by the Center for Research Computing at the University of Kansas supported in part through the NSF MRI Award 2117449.

References

[1] G. Wilson and B. Madison , "Reimagining e^+e^- collider precision luminosity measurements". , this proceedings (2024)

[2] K. Greisen , "Cosmic Ray Showers". Annual Review of Nuclear Science. 10. Laboratory of Nuclear Studies, Cornell University, Ithaca, N. Y.: 71. (1960) https://doi.org/10.1146/annurev.ns.10.120160.000431

[3] N. R. Walter, et al. , "Electron-Induced Cascade Showers in Copper and Lead at 1 GeV". Physical review Vol. 149, Pages 201-208 (1966). http://doi.org/10.1103/PhysRev.149.201

[4] D.E. Groom , S. R. Klein for P.A. Zyla et al. (Particle Data Group), Prog. Theor. Exp. Phys. 2020, 083C01 2021 update (2021).

[5] I. Levy , "Detector R&D towards realistic luminosity measurement at the forward region of future e^+e^- linear colliders". Thesis submitted to Tel Aviv University (2019). https://inspirehep.net/files/5a22206735eb2ffe0e97f5e36d128080

[6] T.C. Awes, et al. , "A Simple method of shower localization and identification in laterally segmented calorimeters" , Nucl. Instrum. Meth. A Vol 311 Pages 130-138 , (1992) https://doi.org/10.1016/0168-9002(92)90858-2

[7] A. Broder, et al. , "Scalable K-Means by Ranked Retrieval" , WSDM'14 (2014) http://dx.doi.org/10.1145/2556195.2556260

[8] D. Virmani, S. Taneja, G. Malhotra , "Normalization based K means Clustering Algorithm" , IJAERS , arxiv[cs.LG]:1503.00900 , (2015) https://doi.org/10.48550/arXiv.1503.00900

[9] H. Abramowicz, et al. , "International Large Detector: Interim Design Report" , (2020) https://doi.org/10.48550/arXiv.2003.01116

[10] R. Wigmans, *Calorimetry Energy Measurement in Particle Physics Second Edition* (Oxford Science Publications, Oxford 2017)

[11] F. Binon, et al. , "HODOSCOPE GAMMA SPECTROMETER GAMS-200" , Nucl. Instrum. Meth. , Vol 188 Pages 507 (1981) https://doi.org/10.1016/0029-554X(81)90261-5

[12] G.Abbiendi, et al. , "Precision Luminosity for Z0 Lineshape Measurements with a Silicon-Tungsten Calorimeter" , Eur.Phys.J.C14 Pages 373-425, (2000) https://doi.org/10.1007/s100520000353

[13] B. F. Philips, et al. , "Development of thick intrinsic silicon detectors for hard X-ray and gamma-ray detection" , IEEE , (2001) https://doi.org/10.1109/NSSMIC.2001.1008442

[14] H. Bethe and W. Heitler , "On the Stopping of Fast Particles and on the Creation of Positive Electrons" , Proceedings of the Royal Society of London. Series A, Containing Papers of a Mathematical and Physical Character Vol. 146, No. 856 , pp. 83-112 , (1934) https://www.jstor.org/stable/2935479

[15] G. R. Lynch, O. I. Dahl, "Approximations to multiple Coulomb scattering" , Nuclear Instruments and Methods in Physics Research Section B: Beam Interactions with Materials and Atoms, Volume 58, Issue 1, 2 May 1991, Pages 6-10 (1991) https://doi.org/10.1016/0168-583X(91)95671-Y

[16] G. Grindhammer, S. Peters , "The Parameterized Simulation of Electromagnetic Showers in Homogeneous and Sampling Calorimeters" , Proceedings of Int. Conf. on Monte Carlo Simulation in High Energy and Nuclear Physics, Tallahassee, Florida, USA, (1993) https://doi.org/10.48550/arXiv.hep-ex/0001020